Role of direct mechanism in two-nucleon $T = 0$ transfer reactions in light nuclei using the (^{6}Li, α) probe

J. C. Zamora [1,*] J. L. Ferreira,[2] A. Barioni [3] E. N. Cardozo [2] D. Abriola,[4] A. Arazi,[4] M. Assunção,[5] E. de Barbará,[4] M. A. Cardona [4] V. Guimarães,[1] D. Hojman [4] G. V. Martí [4] D. R. Mendes, Jr. [2] A. J. Pacheco [4] K. C. C. Pires,[1] D. Ramos,[4] O. C. B. Santos [1] and J. Lubian [2]

[1]*Instituto de Física, Universidade de São Paulo, São Paulo, 05508-090 São Paulo, Brazil*
[2]*Instituto de Física, Universidade Federal Fluminense, Niterói, 24210-340 Rio de Janeiro, Brazil*
[3]*Departamento de Ciências do Mar, Universidade Federal de São Paulo, Santos, 11070-100 São Paulo, Brazil*
[4]*Laboratorio TANDAR, Comisión Nacional de Energía Atómica, BKNA1650 San Martín, Argentina*
[5]*Departamento de Física, Universidade Federal de São Paulo, Diadema, 09913-030 São Paulo, Brazil*

Background: Two-nucleon transfer reactions provide a unique tool to understand the correlation between nucleon pairs. Two-nucleon (*pp*, *nn*, and *np*) transfer reactions can occur via isoscalar ($T = 0$, $S = 1$) or isovector ($T = 1$, $S = 0$) processes. In particular, the isoscalar pair transfer can be induced by the (α, d) or (^{6}Li, α) probes. In the past, most of the isoscalar *np*-transfer studies were performed with the (α, d) reaction, but this probe is strongly momentum mismatched with respect to other two-nucleon transfer reactions.

Purpose: We aim to investigate the interplay between direct and sequential reaction mechanisms from the analysis of experimental (^{6}Li, α) angular distributions in light targets.

Method: Differential cross sections of (^{6}Li, α) reactions at a beam energy of 20 MeV were measured with ^{12}C and ^{19}F targets. The interplay between direct and sequential transfer mechanisms in the experimental angular distributions was investigated with coupled-reaction-channels calculations.

Results: The experimental angular distributions of isoscalar *np* transfer were compared with theoretical calculations assuming a direct or a sequential reaction mechanism. Direct *np*-transfer calculations describe successfully most of the angular distributions. The sequential transfer mechanism is about two orders of magnitude smaller than the direct process.

Conclusions: The present results suggest a significant *np* correlation in the ^{12}C(^{6}Li, α)^{14}N* and ^{19}F(^{6}Li, α)^{21}Ne* reactions. Despite the relatively low cross section for the reactions with the asymmetric ^{19}F target, the direct transfer mechanism remains dominant over the sequential process. Further studies including measurements with other asymmetric *sd*-shell nuclei will be required to fully understand the isoscalar and isovector *np*-transfer mechanism in this nuclear region.

I. INTRODUCTION

Two-nucleon transfer reactions have recently attracted a renewed interest due to their great relevance in studies of short-range correlations and spin-isospin structure in nuclei. In particular, two-nucleon transfer reactions provide a unique tool to understand the interaction between nucleon pairs (*pp*, *nn*, and *np*), which have significant consequences in a large variety of subjects such as neutron stars [1,2], neutrinoless double-β decay [3,4] and collective nuclear vibrations [5,6].

Two-nucleon transfer reactions can occur via direct or sequential processes. The direct process is associated with transferring a nucleon pair in a one-step reaction with certain selection rules. The sequential process involves an interme-diate state that is populated via one-nucleon transfer and is followed by a second-step reaction to transfer a second nucleon. The intermediate system may also involve more than one excited state. Experimentally, both direct and sequential processes can not be separated, but their superposition may have a constructive or destructive interference in the measured cross section [7]. The one-step process can be calculated with the first-order distorted-wave Born approximation (DWBA). Even so, cross sections are usually underpredicted in this approach [8]. Second-order DWBA calculations give a better description of the two-nucleon transfer mechanism by explicitly introducing the sequential transfer [8,9]. However, the existence of strong inelastic excitations may significantly impact the reaction mechanism [10,11]. Therefore, the most consistent method to account for inelastic states in the two-nucleon transfer reaction is the coupled-reaction-channels (CRC) approach. Although the CRC formalism is more robust than DWBA, this method has many advantages for describing the direct and sequential transfer reaction. For instance, a

nonorthogonality term in the CRC calculations is explicitly included [12]. Similarly, the CRC calculations do not require adjustable parameters or normalization factors in the cross section to describe the experimental data.

Selection rules for the transfer of a nucleon pair are characterized by the intrinsic quantum numbers of the transferred cluster: J (total angular momentum), L (orbital angular momentum), S (spin), and T (isospin). Protons and neutrons can be coupled in pairs with different configurations depending on the spin and isospin. For instance, a deuteronlike pair ($T = 0$, $S = 1$) corresponds to an isospin-singlet configuration, while the pp, nn, and np ($T = 1$, $S = 0$) form an isospin triplet. Reaction probes such as (t, p) or (p, t) are strongly selective to populate states with the same initial and final spins with isospin transfer $T = 1$. The (α, d) and (d, α) reactions are pure isoscalar probes that are used to populate states with a spin transfer $S = 1$. The $(^3\text{He}, p)$ and $(p, {}^3\text{He})$ reactions provide both isoscalar and isovector transfers with spin $S = 0$ or 1. Therefore, depending on the selection rules and the internal structure of the nuclei involved in a reaction, a certain probe or a combination of them can be used to investigate isoscalar or isovector two-nucleon transfer. In this work, the isoscalar probe $(^6\text{Li}, \alpha)$ [similar to (α, d)] is used to investigate the deuteronlike transfer off ^{12}C and ^{19}F. Exact finite-range CRC calculations are employed to describe the experimental angular distributions. Both bound and unbound states are included in our calculations.

This paper is organized as follows. In Section II, the experimental conditions are described. Results and data analysis with CRC calculations for both ^{12}C and ^{19}F targets are presented in Sec. III. The effect of direct and sequential transfer mechanisms is also presented in the same Section. In Sec. IV, a discussion of the results and a comparison with other reactions probes is made to evaluate the performance of the $(^6\text{Li}, \alpha)$ reaction in two-nucleon transfer studies. Finally, in Sec. V, we give the main conclusions of our work.

II. EXPERIMENT

Elastic scattering and two-nucleon transfer reactions induced by ^6Li on ^{12}C and ^{19}F targets were measured at the TANDAR facility [13]. A ^6Li beam was produced and accelerated via the 20-UD Tandem accelerator to an energy of 20 MeV in the laboratory frame. The beam intensity was measured in a Faraday cup to be approximately 5 nA. ^6Li particles were transported to a 70-cm-diameter scattering chamber located at the end of the multipurpose beam line. The reaction targets were mounted on a remote-controlled target ladder placed at the center of the scattering chamber. Self-supported foils of $^{\text{nat}}\text{C}$ (1.1 mg/cm^2 thick), polytetrafluoroethylene (Teflon®) [C$_2$F$_4$] (2.6 mg/cm^2 thick) and gold (170 μg/cm^2 thick) were used in the experiment.

The detector setup was composed of an array of eight surface-barrier detectors (150 μm thick) and four silicon telescope detectors ΔE(25 μm)-E_R(150 μm) covering scattering angles from 10° to 62°. The surface-barrier detectors were collimated with rectangular slits, defining an angular acceptance smaller than 0.4°, and solid angles ranged from 0.3 msr (most forward detector) to 0.7 msr (most backward detector).

The silicon telescopes were mounted on the side opposite (relative to the beam axis) to the surface-barrier detector array with an angular separation of 10° between adjacent detectors. The solid angle covered by each detector was around 0.3 msr. These detectors allowed the identification of the reaction products measured in the experiment. The normalization of the cross section was performed using a luminosity monitor that was mounted at a fixed angle of 16° with a solid angle of 0.02 msr. The readout of this detector was made with a digitizer that allows to extract the count rate in small time intervals, which improves the sensitivity to beam-current fluctuations. Calibration runs with a gold target were used to normalize the count rate of this detector with the Rutherford cross section. The cross sections were obtained with the luminosity monitor data and the respective solid angle and total events in each silicon detector. The systematic uncertainty in the absolute cross sections determined with this procedure was estimated to be 4%, which was dominated by the readout accuracy of the luminosity monitor in the calibration runs. The statistical uncertainty was below 5% for most of the data, except for the measurements with ^{19}F that have a typical uncertainty at the level of 20%.

Figure 1(a) shows an example particle-identification spectrum for the $^6\text{Li} + {}^{12}\text{C}$ collision measured with a telescope detector at $\theta_{\text{lab}} = 27°$. As can be seen, several reaction products like p, d, α and ^6Li are separated by different bands. For instance, the ^6Li band shows the elastic scattering and the first 2^+ excited state of ^{12}C. The small bumps close to the elastic scattering peak originate from target impurities (mainly oxygen and calcium) of less than 5%. The projectile breakup and $^{12}\text{C}(^6\text{Li}, \alpha){}^{14}\text{N}$ reaction channels are extracted from the α band. Figure 1(b) shows a projection of this band on the ^{14}N excitation energy. As can be noticed, several excited states in ^{14}N were populated via np-transfer reactions. The energy resolution achieved was around 400 keV FWHM (full width at half maximum). Measurements of np transfer from ^{19}F were performed using a Teflon target. Reactions on carbon were subtracted from measurements with the $^{\text{nat}}\text{C}$ target using the respective normalizations.

III. RESULTS

In this work, the analysis of isoscalar np transfer in the $^{12}\text{C}(^6\text{Li}, \alpha){}^{14}\text{N}$ and $^{19}\text{F}(^6\text{Li}, \alpha){}^{21}\text{Ne}$ stripping reactions ($E_{\text{lab}} = 20$ MeV) was performed with exact finite-range CRC calculations. As the nucleon pair transfer can take place in both direct and sequential processes, detailed calculations for each reaction mechanism are presented in this section. On the one hand, a deuteronlike particle ($T = 0$, $S = 1$) is transferred to the target nucleus (^{12}C or ^{19}F) in a one-step reaction. On the other hand, the np-pair can be transferred through a sequential mechanism involving intermediate states. In the latter case, independent of which particle (proton or neutron) is transferred first, the intermediate reaction involves an unbound ejectile nucleus (^5Li or ^5He). However, we can assume that the ejectile particle can survive for a very short period of time to make a secondary reaction. A detailed discussion of the role of direct and sequential np-transfer mechanisms in the $^6\text{Li} + {}^{12}\text{C}$ and $^6\text{Li} + {}^{19}\text{F}$ systems is presented below. Finally, the interplay
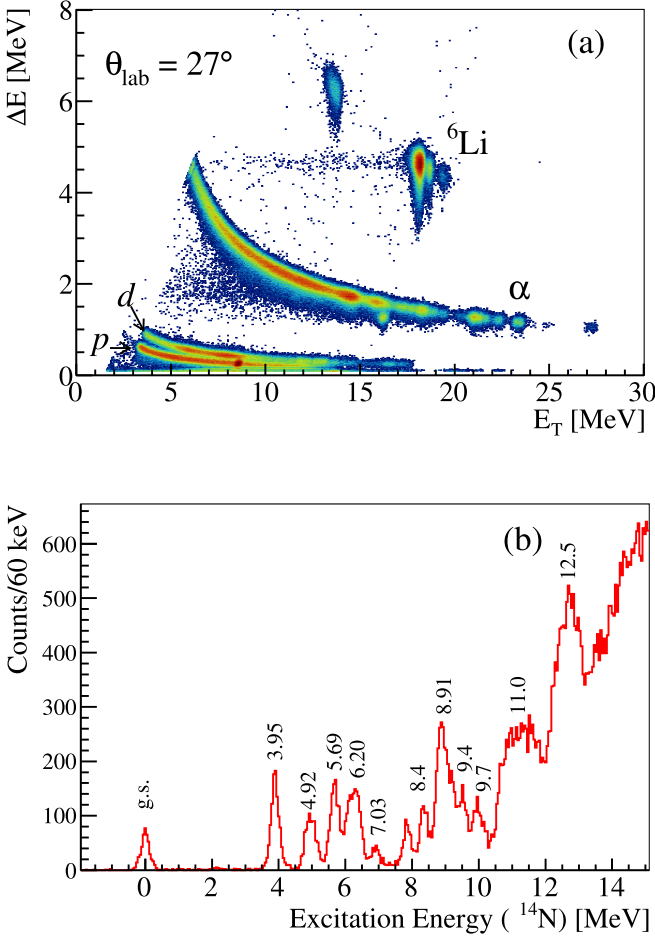
FIG. 1. (a) Particle identification spectrum for the ^{6}Li + ^{12}C collision obtained from a telescope detector at $27°$ in the laboratory system. E_T corresponds to the total energy deposited in the telescope detector, which is given by $\Delta E + E_R$. (b) The projected energy of the α particles in the excitation energy of the ^{14}N residual nucleus.

between direct and sequential transfer mechanisms will provide important information about the pairing correlation between protons and neutrons in the reaction process.

A. Direct isoscalar np-transfer reaction

In the direct np transfer, the ^{6}Li projectile is assumed to be a cluster composed by a deuteronlike particle (isoscalar np pair) orbiting an α core. In this approach, a np pair is transferred to a target nucleus and populates excited states in a residual nucleus (^{14}N or ^{21}Ne). The respective spectroscopic amplitudes for the wave functions of the two-valence nucleons were determined from shell-model calculations using the code NUSHELLX [14]. The approach here presented, named the microscopic-cluster model, was also considered in the analysis of a two-neutron transfer in the ^{12}C(^{18}O, ^{16}O) ^{14}C stripping reaction at 84 MeV [15]. The calculations were carried out considering the effective Hamiltonian derived by McGlory and Wildenthal [16]. This effective Hamiltonian was properly built for a model space in which the valence protons and neutrons populate the active orbits $p_{1/2}$, $d_{5/2}$, and $s_{1/2}$ with the

single-particle energies $\epsilon_{p_{1/2}} = -5.696$ MeV, $\epsilon_{d_{5/2}} = -1.668$ MeV, and $\epsilon_{s_{1/2}} = -2.840$ MeV. Moreover, the ^{12}C nucleus is regarded as a closed core. The one and two-body matrix elements were obtained by a least-squares fitting, where the calculated ground and excited states were fitted to describe the experimental data of nuclei in the mass region $A = 13$–22.

A canonical transformation of coordinates to the spectroscopic amplitudes was performed. The individual coordinates of both valence particles were converted into the relative motion coordinate (between the valence proton and neutron) and the center-of-mass coordinate of the n-p system relative to the core. Thus, the spectroscopic amplitude for the np-pair wave function is given by [17]

$$S_{\alpha J \beta J'}[(nl)(NL)\Lambda S; J]$$

$$= \sum_{n_1 l_1 n_2 l_1} \sum_{j_1 j_2} \hat{S}\hat{L}\hat{j}_1\hat{j}_2 \begin{Bmatrix} l_1 & 1/2 & j_1 \\ l_2 & 1/2 & j_2 \\ \Lambda & S & J \end{Bmatrix} C^L(n_1 l_1 n_2 l_2; nlNL)$$

$$\times S_{\alpha J \beta J'}[n_1 l_1 j_1 n_2 l_2 j_2; J]. \tag{1}$$

Above, $S_{\alpha J \beta J'}[n_1 l_1 j_1 n_2 l_2 j_2; J]$ is the two-particle spectroscopic amplitude determined from the shell-model calculation considering the jj-coupling. $\hat{\zeta} = \sqrt{2\zeta + 1}$ with $\zeta = S, L, j_1, j_2$. The expressions between braces are the $9j$ coefficients, and $C^L(n_1 l_1 n_2 l_2; nlNL)$ stands for the Moshinsk brackets [18]. The quantum numbers to specify the cluster wave function, such as the principal quantum number and orbital angular momentum, were determined by considering the conservation of total quanta number ($\mathcal{N}$) in the transformation from the individual particle coordinates to the coordinates in the cluster space. Then, $\mathcal{N} = 2(N-1) + L + 2(n-1) + l = 2(n_1-1) + l_1 + 2(n_2-1) + l_2$ is satisfied. (N, L) and (n, l) are the quantum numbers of the wave functions that describe the movement of the center of mass of the np cluster around the core and the coordinate of the relative motion between the proton and neutron that compose the np pair, respectively. (n_i, l_i), with $i = 1, 2$, are the quantum numbers of the single-particle wave functions.

In the present work, $n = 1$ and $l = 0$ are assumed for the intrinsic state of the isoscalar np pair. In the Appendix, Tables IV and V present the resulting spectroscopic amplitudes for the valence np cluster, considering the active orbits $p_{1/2}$, $d_{5/2}$, and $s_{1/2}$ as model space for both proton and neutron. It is important to note that the model space used allows states with positive and negative parities. The next part of our analysis corresponds to the construction of the optical model (OM) potentials.

1. Optical potentials

OM potentials are one of the ingredients needed to perform transfer-reaction calculations. Considering a stripping reaction in which one particle (or structureless cluster), v, is transferred from a projectile ($a = b + v$) to a target nucleus (A), the respective transfer-matrix elements for the reaction $a + A \Longrightarrow b + B$, with $B = A + v$, is given by

$$T_{\alpha\beta} = \langle \Psi_\beta^{(-)} | U_{bA}(\mathcal{R}') + v_{vA}(\mathbf{r}) - U_{aA}(\mathbf{R}) | \Psi_\alpha^{(+)} \rangle. \tag{2}$$
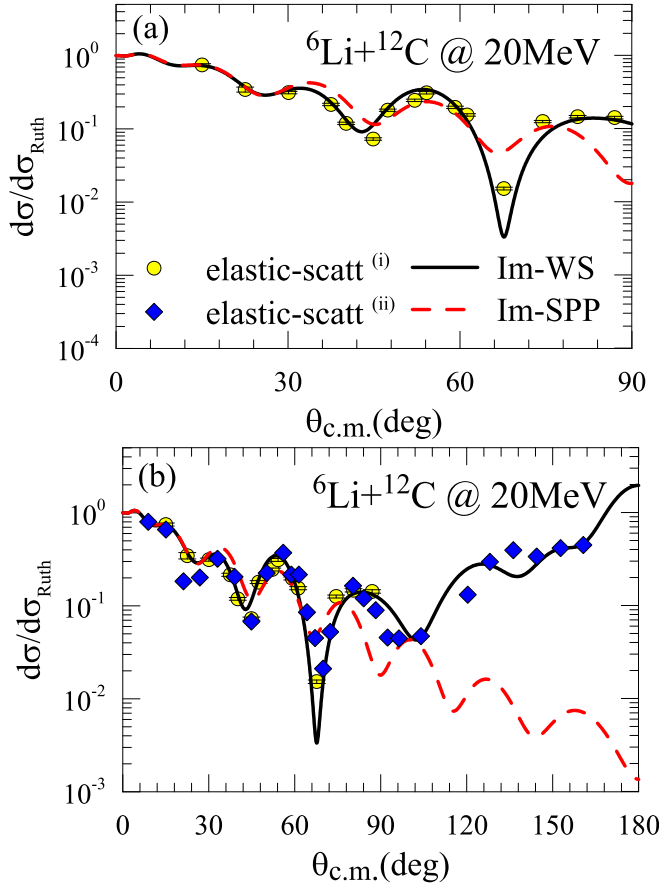
FIG. 2. Single-channel calculations for the ^{12}C(^{6}Li, ^{6}Li)^{12}C reaction at 20 MeV incident energy. (i) the elastic-scattering data of the present work. (ii) the elastic-scattering data from Ref. [22]. (a) and (b) are the same figure but plotted with different ranges.

FIG. 3. Single-channel calculations for the ^{19}F(^{6}Li, ^{6}Li)^{19}F reaction at 20 MeV incident energy. (a) and (b) are the same figure but plotted with different ranges.

$U_{bA}(\mathcal{R}')$ and $U_{aA}(\mathbf{R})$ are complex potentials that are defined to describe the elastic scattering between the core (b) and target (A), and projectile (a) and the target (A) nuclei, respectively. Moreover, $v(\mathbf{r})$ is a real potential, which binds the valence particle (or structureless valence cluster) to the core nucleus. $\Psi_\alpha^{(+)}$ and $\Psi_\beta^{(-)}$ are the total wave functions of the initial and final partitions, for which superscripts $(-)$ and $(+)$ mean the asymptotic ingoing and outgoing wave functions, respectively. In the DWBA approach, $U_{bA}(\mathcal{R}')$ and $U_{aA}(\mathbf{R})$ are chosen to describe the elastic scattering between $b + A$ and $a + A$, respectively. Then, the two-nucleon transfer is treated as a second-order process.

The OM potential used in the CRC calculations is based on the São Paulo potential (SPP) [19]. In order to test the capability of the SPP to describe the elastic scattering of the ^{6}Li + ^{12}C and ^{6}Li + ^{19}F systems, single-channel OM calculations were performed. In this approach, an OM potential is constructed with the SPP using normalization coefficients for the real (1.0) and imaginary (0.78) parts as $U(R) = (1.0 + 0.78i)V_{SP}^{LE}(R)$. The systematic coefficient 0.78, for the imaginary part, has been shown to describe elastic scattering in the energy region where couplings to the elastic channel are not relevant [20,21]. Figures 2(a) and 3(a) show the angular distributions up to
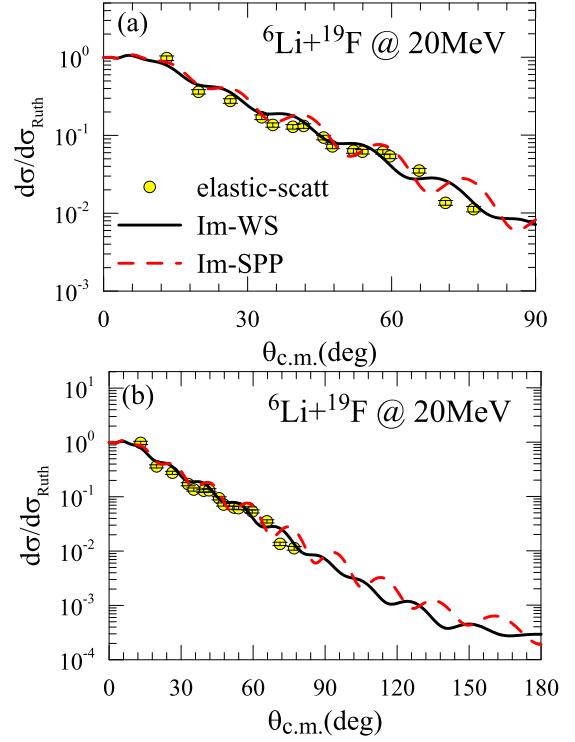
$\theta_{\text{c.m.}} = 90°$ for the elastic scattering of both ^{6}Li + ^{12}C and ^{6}Li + ^{19}F collisions, respectively.

As can be noticed, the SPP (dashed red line) provides a reasonably good agreement of the elastic scattering compared to the experimental data. However, it is well known from previous experiments (see for example Ref. [22]) that the elastic-scattering cross section, for the ^{6}Li + ^{12}C system, has a different trend above 90° than the SPP prediction [Fig. 2(b)]. Experimental data from Ref. [22] ($E_{\text{lab}} = 20$ MeV) were also included in Fig. 2(b) for comparison. As can be seen, the experimental cross section increase at backward scattering angles. This effect has also been reported for other light systems such as ^{4}He + ^{12}C, ^{4}He + ^{14}N, ^{4}He + ^{16}O [23], ^{9}Be + ^{12}C [22], ^{16}O + ^{12}C [24,25], and ^{7}Be + ^{9}Be [26]. In the last three systems, the elastic-transfer reaction channel

TABLE I. Parameters of the spin-orbital interaction and imaginary part of the optical potential used in the single-channel OM calculations.

| System	W (MeV)	r_w (fm)	a_w (fm)
^{6}Li + ^{12}C	6.03	1.293	0.76
^{6}Li + ^{19}F	19.0	1.230	0.97
System	$V_{s.o.}$ (MeV)	$r_{s.o.}$ (fm)	$a_{s.o.}$ (fm)
^{6}Li + ^{12}C	1.00	1.16	0.65
^{6}Li + ^{19}F	2.00	1.16	0.65

TABLE II. Parameters of the spin-orbital interaction and imaginary part of the OM potential used in the transfer reaction calculations with a ^{12}C target.

System	W (MeV)	r_w (fm)	a_w (fm)
^{6}Li + ^{12}C	10.6	1.103	0.56
^{4}He + ^{14}N	5.66	0.900	0.60

System	$V_{s.o.}$ (MeV)	$r_{s.o.}$ (fm)	$a_{s.o.}$ (fm)
^{6}Li + ^{12}C	1.00	1.16	0.65
^{4}He + ^{14}N	1.84	1.32	0.45

also contributes at the backward angular region of the cross section [22,25,26]. Therefore, the theoretical results for the elastic-scattering derived by the SPP, with a 0.78 coefficient in the imaginary part, do not reproduce the trend at backward angles for the ^{6}Li + ^{12}C system. This might be explained due
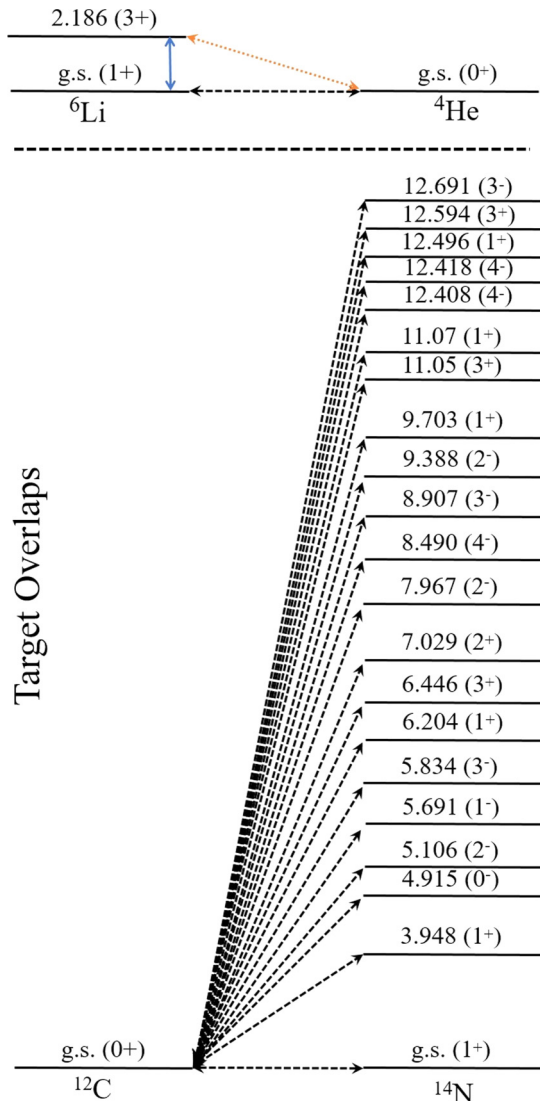
FIG. 4. Coupling scheme considered for the projectile and target overlaps in the ^{12}C(^{6}Li, α) ^{14}N reaction.
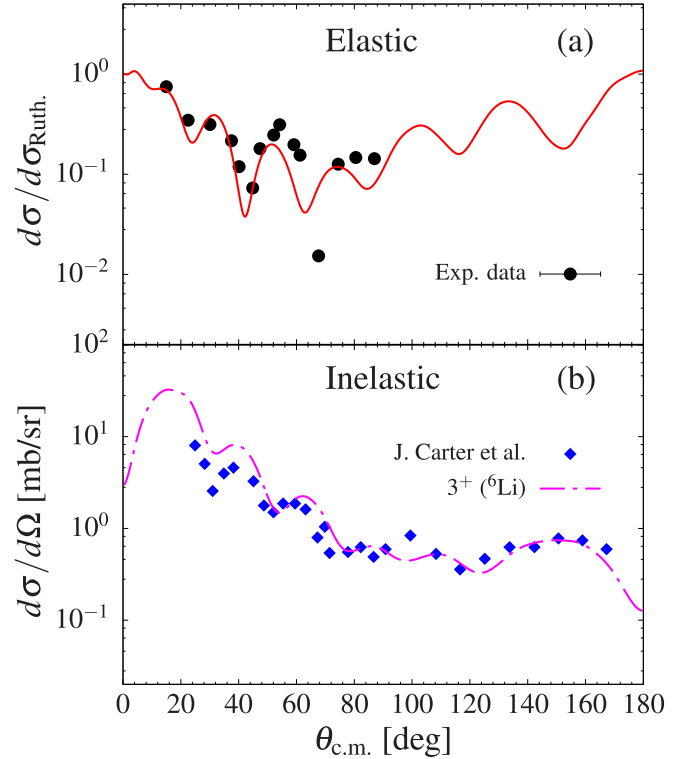
FIG. 5. Elastic-scattering angular distribution, for the ^{6}Li + ^{12}C collision, obtained from CRC calculations (a). The inelastic-scattering angular distribution for the projectile excitation to the first 3^+ (2.19 MeV) state was obtained from the CRC calculations (b). The inelastic scattering data were extracted from Ref. [22].

to the fact that the SPP is a double-folding interaction which is very absorbing at the nuclear interior. Thus, collisions with very small impact parameters feel a stronger nuclear potential removing too much flux from the elastic scattering channel. In order to properly describe the experimental data at backward angles, the imaginary part of the OM was replaced by a shallow Woods-Saxon potential and a real spin-orbit term considering the parameters given in Table I. The resulting elastic-scattering cross section using this hybrid potential is presented in Fig. 2 with a black solid line [see panels (a) and (b)]. Now, the angular distribution below 90° is slightly improved, and the increase in the cross section at backward angles is well reproduced.

The situation for the ^{6}Li + ^{19}F elastic scattering is somewhat different from the theoretical point of view (see Fig. 3). The predicted differential cross section for this system remains decreasing above 90°, even with the hybrid OM potential (see Table I). Experimental data for this system are very scarce, so no data at backward angles were found in the literature to compare with our results. However, measurements of ^{6}Li backscattering on ^{19}F were reported in Ref. [27]. The elastic scattering cross section at $\theta_{c.m.} = 150°$ was measured at incident energies from 2.5 to 7 MeV. The ratio of the experimental and Rutherford cross sections decreases rapidly with the beam energy, in particular above the Coulomb barrier. It is clear that the energies covered in Ref. [27] are at least a factor 3 smaller than our experimental data, but the

TABLE III. Parameters of the spin-orbital interaction and imaginary part of the optical potential used in the transfer calculations with a ^{19}F target.

System	W (MeV)	r_w (fm)	a_w (fm)
^{6}Li + ^{19}F	12.0	1.03	1.07
System	$V_{s.o.}$ (MeV)	$r_{s.o.}$ (fm)	$a_{s.o.}$ (fm)
^{6}Li + ^{19}F	1.00	1.16	0.65

overall trend of the backscattering cross section suggests that the angular distribution above $90°$ should decrease for higher incident energies.

2. One-step ^{12}C(^{6}Li, α) ^{14}N* reaction

Exact finite-range CRC calculations were performed using the code FRESCO [12,28]. As explained above, the OM potentials used in the calculations were composed of the SPP [19] and Woods-Saxon interactions for the real and imaginary parts, respectively. These hybrid OM potentials were employed to properly account for the elastic-scattering cross sections in the ^{6}Li + ^{12}C and ^{4}He + ^{14}N systems. In contrast to the single-channel calculation presented in the previous section, several excited states in ^{14}N were coupled in the calculation. As the experimental data comprised also unbound (resonance) states, opened-transfer channels were explicitly included to solve the coupled equations. In this case, the imaginary part of the OM potential was renormalized in order to reduce the absorption of flux, and to avoid double counting. The parameters in Table II were considered for the imaginary part of the respective OMs. These Woods-Saxon interactions account for the dissipative processes concerning the still missing couplings, such as the breakup process of the projectile ^{6}Li in the initial partition and couplings among the states of the ^{14}N nucleus in the final partition. The core-core (^{4}He + ^{12}C) OM potential was obtained from the SPP interaction with the normalization coefficients set to $U(R) = (1.0 + 0.78i)V_{SP}^{LE}(R)$. The post representation was considered to determine the transfer-matrix elements using complex remnant terms of the potential. The respective nonorthogonality terms were also included in the calculation.

The coupling scheme considered for the target overlaps in the isoscalar np-transfer calculation is presented in Fig. 4. In total, 21 (9 bound and 12 unbound) states in ^{14}N were assumed for the CRC calculation. The spectroscopic amplitudes for the valence particle (deuteronlike particle) are given in Table IV (see Appendix). The spectroscopic amplitudes for excited states above the proton separation energy ($S_p = 7.55$ MeV) were assumed to be equal to 1. The spectroscopic factors (SFs) for the valence np-cluster in the ^{6}Li ground state were extracted from Ref. [29]. SF = 0.69 and SF = 0.04 were used in the calculations for the $L = 0$ and $L = 2$ components, respectively. These spectroscopic factors are consistent to the ones reported in other works [30,31]. The coupling scheme also involved a projectile (^{6}Li) excitation of the first 3^+ resonant state at 2.19 MeV. The Coulomb and nuclear potentials were deformed for the description of this excited state. A

TABLE IV. Spectroscopic amplitudes for the projectile and target overlaps wave functions considered in the d-transfer calculation in the ^{12}C(^{6}Li, ^{4}He) ^{14}N reaction.

Initial state	N	L	S	J	Final state	S.A.
^{12}C$_{g.s.}$(0^+)	2	0	1	1	^{14}N$_{g.s.}$(1^+)	0.134
^{12}C$_{g.s.}$(0^+)	1	2	1	1	^{14}N$_{g.s.}$(1^+)	−0.599
^{12}C$_{g.s.}$(0^+)	3	0	1	1	^{14}N$_{g.s.}$(1^+)	0.040
^{12}C$_{g.s.}$(0^+)	2	2	1	1	^{14}N$_{g.s.}$(1^+)	0.016
^{12}C$_{g.s.}$(0^+)	2	0	1	1	^{14}N$_{3.95}$(1^+)	−0.005
^{12}C$_{g.s.}$(0^+)	1	2	1	1	^{14}N$_{3.95}$(1^+)	0.024
^{12}C$_{g.s.}$(0^+)	3	0	1	1	^{14}N$_{3.95}$(1^+)	0.504
^{12}C$_{g.s.}$(0^+)	2	2	1	1	^{14}N$_{3.95}$(1^+)	−0.055
^{12}C$_{g.s.}$(0^+)	2	1	1	0	^{14}N$_{4.92}$(0^-)	−0.646
^{12}C$_{g.s.}$(0^+)	2	1	1	2	^{14}N$_{5.11}$(2^-)	−0.400
^{12}C$_{g.s.}$(0^+)	1	3	1	2	^{14}N$_{5.11}$(1^-)	−0.153
^{12}C$_{g.s.}$(0^+)	2	1	1	1	^{14}N$_{5.69}$(3^-)	0.527
^{12}C$_{g.s.}$(0^+)	1	3	1	3	^{14}N$_{5.83}$(1^+)	0.577
^{12}C$_{g.s.}$(0^+)	2	0	1	1	^{14}N$_{6.20}$(1^+)	−0.024
^{12}C$_{g.s.}$(0^+)	1	2	1	1	^{14}N$_{6.20}$(1^+)	0.107
^{12}C$_{g.s.}$(0^+)	3	0	1	1	^{14}N$_{6.20}$(1^+)	0.022
^{12}C$_{g.s.}$(0^+)	2	2	1	1	^{14}N$_{6.20}$(3^+)	0.101
^{12}C$_{g.s.}$(0^+)	2	2	1	3	^{14}N$_{6.45}$(2^+)	0.540
^{12}C$_{g.s.}$(0^+)	2	2	1	2	^{14}N$_{7.03}$(1^+)	−0.342

$B(E2; 1^+ \rightarrow 3^+)$ value of 21.8 e^2fm^4 [32–34] was used in the calculations. Moreover, a quadrupole deformation parameter of $\beta_2 = 1.51$ was considered in the couplings of the $1^+ \rightarrow 3^+$ transition and reorientation of the 3^+ excited state [32]. The quadrupole deformation parameter used for the ground-state reorientation was $\beta_2 = -0.079$ [32]. A SF = 1.0 value was adopted for the $\langle ^6$Li*$(3^+)|^4$He$(0^+)\rangle$ overlap.

The predicted angular distributions for the elastic and inelastic scattering obtained from the CRC calculation are presented in Fig. 5. The effect due to the fully coupling configuration in the angular distribution for the elastic scattering, in comparison with the single-channel calculation, is observed mostly at angles above $30°$. Even so, the predicted cross section is still in good agreement with the experimental data. Also, the agreement between theoretical prediction and experimental data for the projectile 3^+ (2.19 MeV) excited state is remarkable. The experimental angular distributions for the low-lying states in ^{14}N populated via isoscalar np transfer are shown in Fig. 6. The results of the CRC calculation for each state are also presented in the figure. In general, the agreement between theory and experiment is quite good, despite of the simplicity of the adopted model. As can be noticed, the agreement with the experimental data for the 1^+ states ($L = 0$) is fairly good. Given that the experimental energy resolution was about 400 keV, a few states between 5 and 7 MeV were not able to be separated in the data. However, the contribution of those states which were not well separated can still be disentangled by considering the respective predicted cross sections. For example, the angular distribution at 5.7 MeV [Fig. 6(d)] shows that the experimental angular distribution has a contribution of both 1^- (5.69 MeV) and 3^- (5.83 MeV) excited states. The incoherent sum of both contributions describes the experimental data, in particular for
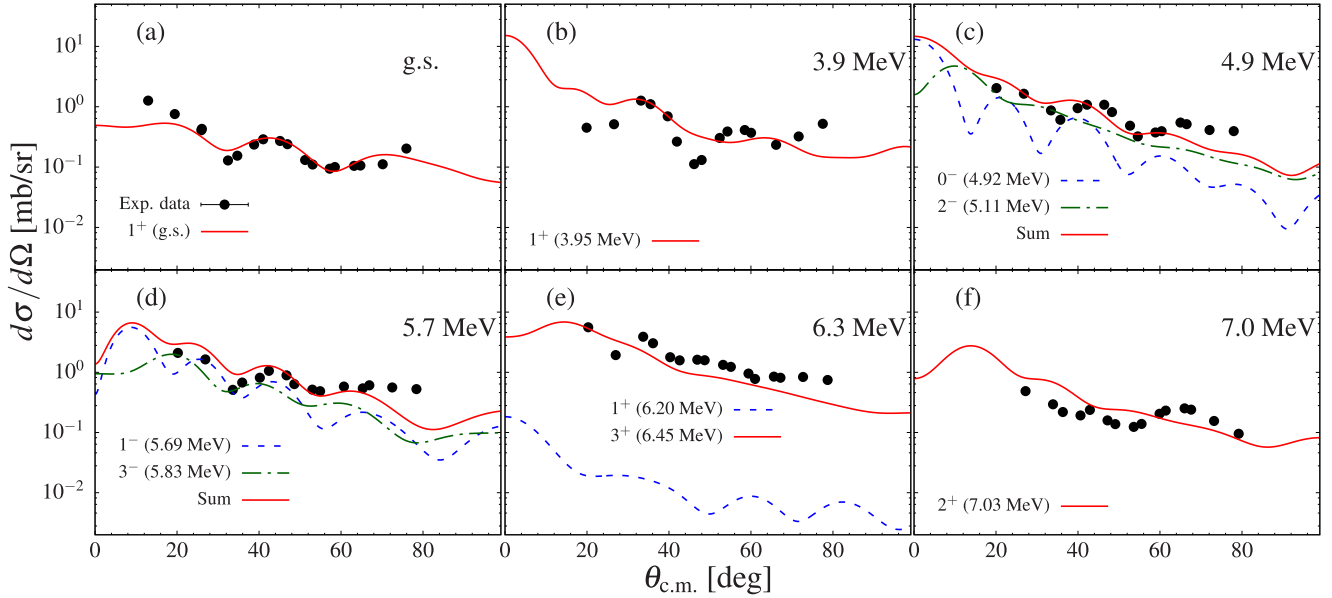
FIG. 6. Experimental angular distributions of the ^{12}C(^{6}Li, α) ^{14}N reaction for several bound states in ^{14}N. The curves are the prediction from CRC calculations. See text for details.

the most backward angles. Similarly, the angular distribution at 6.3 MeV [Fig. 6(e)] is very well reproduced by the 3^+ (6.45 MeV) state that is dominant over the 1^+ (6.20 MeV). For the 2^+ state at 7.05 MeV, the predicted angular distribution slightly overestimates the experimental data (7.0 MeV), but it is still in a reasonable agreement.

It is important to mention that the 0^- (4.92 MeV) excited state is an unnatural parity transition that is not only characterized by the intrinsic state of a deuteronlike particle with $n = 1$ and $l = 0$, but also other configurations might contribute to populate this state. In order to investigate the role of different valence-deuteron wave functions on the transfer reaction, a $^3D_1$ part was introduced in the wave function of the relative motion of the np pair. The resulting contributions of the intrinsic s wave (blue dashed curve) and d wave (green dash-dotted curve) are shown in Fig. 7. As can be noticed, considering
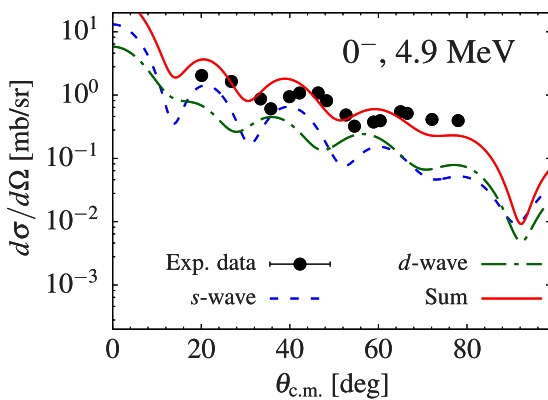
both intrinsic states improves the agreement between theory and experiment, although the oscillation pattern exhibits a 7° shift to lower angles.

The angular distributions for the excited states in ^{14}N above the proton separation energy ($S_p = 7.55$ MeV) are shown in Fig. 8. The theoretical predictions for the direct np-transfer cross sections are presented in the same figures. As can be noticed, the predictions for the 4^- (8.49 MeV), 2^- (9.39 MeV), and 1^+ (9.70 MeV) states [Figs. 8(a), 8(b), and 8(c)] slightly overestimate the experimental angular distributions, mostly at forward angles. This is probably related to the assumption of spectroscopic amplitudes for these states being set to 1. On the other hand, the shapes of the theoretical angular distributions for the unnatural parity states 2^- (9.39 MeV) [Fig. 8(c)] and 1^+ (9.70 MeV) [Fig. 8(d)] reproduce the experimental trend when the transferred angular momentum is assumed to be $L = 3$ and $L = 2$, respectively.

Considering that the excited states at 11 and 12.5 MeV [see Figs. 8(e) and 8(f)] are above the deuteron separation energy ($S_d = 10.27$ MeV), the overlap wave functions $\langle^{12}$C$|^{14}$N$\rangle$ can be represented by narrow bins in the continuum space. Each bin state, with eigenvalue of energy ϵ_α and width $\delta\epsilon_\alpha$, is generated by a superposition of scattering states of the composite system ^{12}C$+d$, so that the averaged radial wave function is given by

$$\varphi_\alpha(r) = \frac{1}{N_{\epsilon_\alpha}} \int_{\epsilon_\alpha^-}^{\epsilon_\alpha^+} \Gamma_\alpha(\epsilon) u_\epsilon(r) d\epsilon. \tag{3}$$

$\Gamma_\alpha(\epsilon)$ is a weight function centered in ϵ_α and the normalization constants N_{ϵ_α} are defined by $N_{\epsilon_\alpha}^2 = \int_{\epsilon_\alpha^-}^{\epsilon_\alpha^+} [\Gamma_\alpha(\epsilon)]^2 d\epsilon$ [35–38]. The orbital angular momentum L of the bin states must satisfy the parity and momentum conservation intrinsic to the transfer mechanism. Bin widths were carefully chosen so that the lower limit of one bin
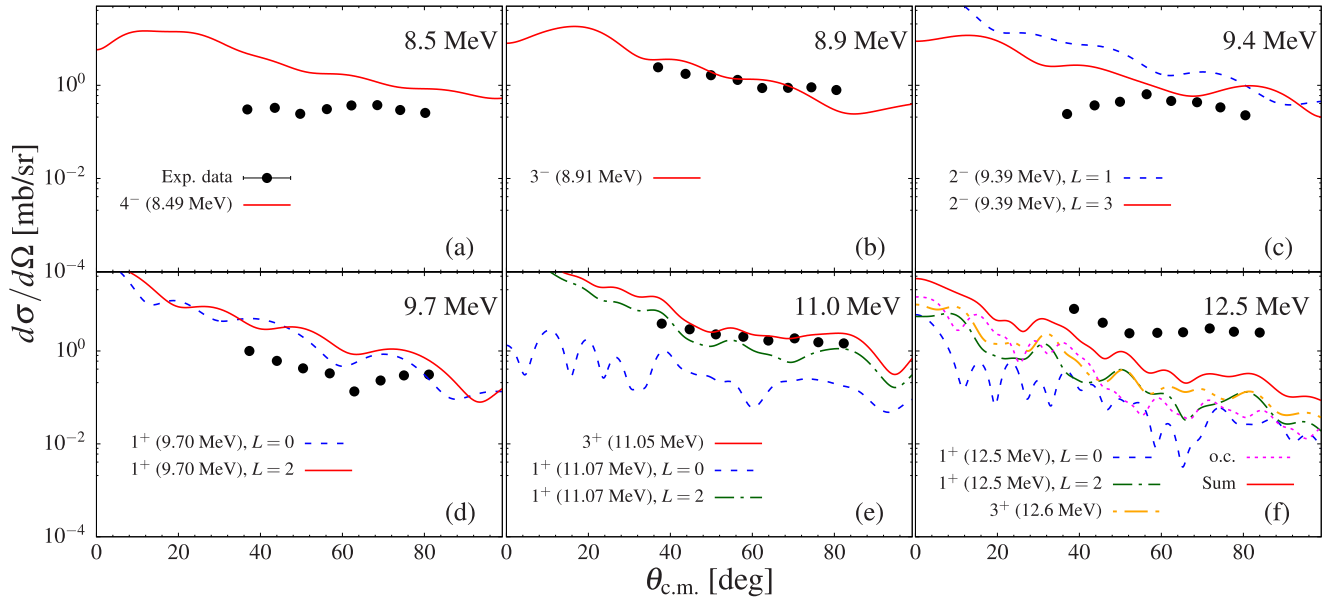

FIG. 7. The contribution of the intrinsic s and np wave functions of the deuteron valence for the transfer differential cross section of the ^{4}He$_{g.s.}(0^+) + {}^{14}$N$_{4.92}(0^-)$ channel. See text for details.

FIG. 8. Experimental angular distributions of the ^{12}C(^{6}Li, α)^{14}N reaction for several unbound states in ^{14}N (above the proton separation energy, $S_p = 7.55$ MeV). The curves are the prediction from CRC calculations. Other components (o.c.) such as the 4^- (12.41 MeV), 4^- (12.42 MeV), and 3^- (12.70 MeV) unbound states were included in the angular distribution at 12.5 MeV (f). See text for details.

coincides with the upper limit of the next bin state. For instance, the excited states with eigenvalues of energies equal to 11.05 and 11.07 MeV were described by bins of $\delta\epsilon_\alpha = 0.02$ MeV with total angular momenta $J = 3$ and $J = 1$, respectively. A similar procedure was used to predict the angular distribution at $E_x = 12.5$ MeV in Fig. 8(f). As can be seen, the agreement between theory and experiment for the angular distributions of the states above the deuteron separation energy is fairly good. However, it is clear that contributions from other excited states might be missing in the calculation for this relatively high-excitation energy range to better describe the experimental angular distribution.

3. One-step ^{19}F(^{6}Li, α) ^{21}Ne* reaction

The procedure for the isoscalar np-transfer reaction analysis in the ^{6}Li + ^{19}F system was similar to the one adopted in the previous section for the ^{12}C data. However, the ^{19}F nucleus brings an extra challenge due to the complexity of its nuclear structure. As ^{19}F is an odd-mass nucleus, several low-lying excited states are located close to its ground state; in particular, the first two excited states are below $E_x = 200$ keV. Therefore, the couplings with inelastic states in the target nucleus can play a significant role in the direct transfer mechanism.

Similarly, finite-range CRC calculations were performed to obtain the isoscalar np-transfer cross sections. The real part of the OM interaction in the initial partition was calculated using the double-folding SPP potential. The imaginary part was obtained from a Woods-Saxon potential with the parameters presented in Table III. These parameters were slightly modified from the single-channel calculation (Table I) to reduce the absorption range from the imaginary potential due to a few inelastic channels in the entrance partition and couplings with transfer channels that were explicitly included. Thus, the

OM potential in the initial partition, presented in Table III, provides a very well description of the elastic scattering of the ^{6}Li + ^{19}F system, as can be observed in Fig. 9. For the final partition (^{4}He + ^{21}Ne) and core-core interaction (^{4}He + ^{19}F), the SPP was used in both real and imaginary parts of the OM potential. The usual strength coefficients $N_r = 1.0$ and $N_i = 0.78$ were considered. The imaginary part absorbs the flux corresponding to opened channels that are not explicitly included in the solutions of the coupled-reaction-channels system of equations [20,21].

The coupling scheme for the projectile and target overlaps considered in the calculations is shown in Fig. 10. The spectroscopic amplitudes for the np-valence pair are given in Table V (Appendix). First, couplings with the ^{19}F ground state (dashed black arrows in Fig. 10) were considered in the calculation. Then, couplings with two excited states in
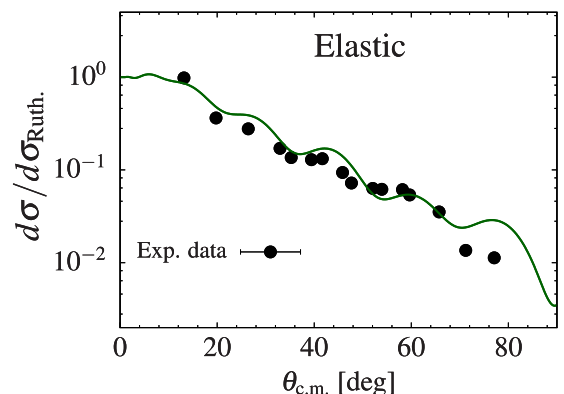

FIG. 9. Elastic-scattering angular distribution, for the ^{6}Li + ^{19}F collision, obtained from CRC calculations.
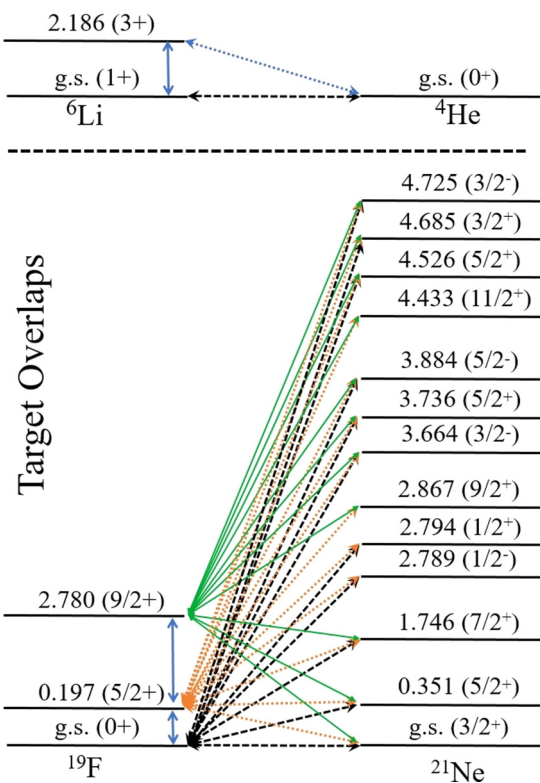
FIG. 10. Coupling scheme considered for the projectile and target overlaps in the $^{19}\text{F}(^6\text{Li}, \alpha)^{21}\text{Ne}$ reaction.

^{19}F (dotted brown and full green arrows in Fig. 10) were introduced to verify their effect on the angular distributions. The $5/2^+$ and $9/2^+$ states in ^{19}F with excitation energies of 197 and 2780 keV, respectively, were considered in this procedure. The quadrupole deformation parameter $\beta_2 = 0.46$ [39] was used to deform the Coulomb and nuclear potentials, and to derive the reduced electric and nuclear matrix elements which connect the target ground state to the $5/2^+$ state within the rotational model. Similarly, a quadrupole deformation of $\beta_2 = 0.42$ [39] was considered in the $^{19}\text{F}_{2.780}(9/2^+) \rightarrow {}^{19}\text{F}_{0.197}(5/2^+)$ transition.

The experimental angular distributions of the $^{19}\text{F}(^6\text{Li}, \alpha)^{21}\text{Ne}^*$ reaction are shown in Fig. 11. The theoretical predictions for each state are also included in this plot. As can be observed, a reasonable good agreement with the experimental data is achieved with the present CRC calculations. Due to the experimental energy resolution (400 keV), more than one excited state in ^{21}Ne may be contributing in the experimental angular distributions. For example, the ground state and the first excited state are off by only 351 keV. Therefore, a way to disentangle the different contributions is to explicitly couple these states to describe the data with a incoherent sum of angular distributions. For instance, the experimental cross section of the np transfer to the ^{21}Ne ground state [shown in Fig. 11(a)] is described after including the angular distribution of the $5/2^+$ state at 351 keV. The only state around $E_x = 1.7$ MeV is the $7/2^+$ (1.75 MeV), so just the prediction of this state is able to describe the experimental data [see Fig. 11(b)]. The theoretical prediction is also in agreement with the angular distribution at 2.7 MeV. The dominant component $1/2^+$ (2.79 MeV) [Fig. 11(c)] describes the data below 40°. The other components $1/2^-$ (2.79 MeV) and $9/2^+$ (2.87 MeV) have a small contribution to the cross section, mostly at larger angles. For the angular distributions corresponding to the experimental peaks at 3.7 and 4.5 MeV [Figs. 11(d) and 11(e)], the theoretical predictions
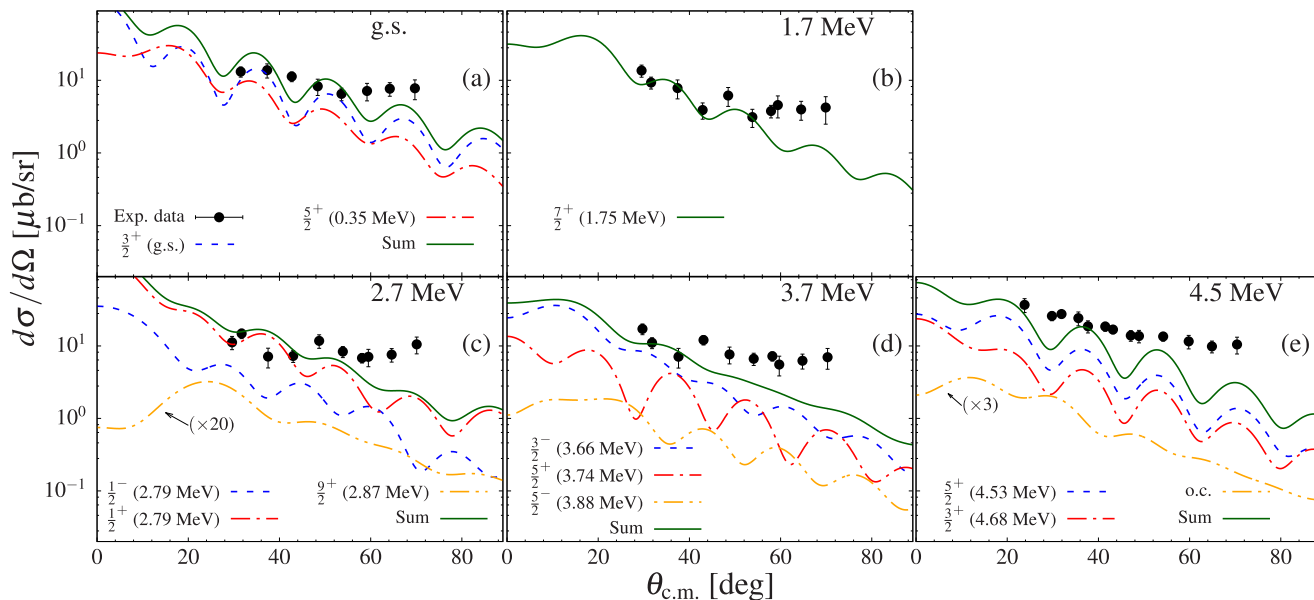
FIG. 11. Experimental angular distributions of the $^{19}\text{F}(^6\text{Li}, \alpha)^{21}\text{Ne}$ reaction populating a few states in ^{21}Ne. The curves are the prediction from CRC calculations. Note that the lower angular distributions at 2.7 (c) and 4.5 MeV (e) were scaled by factors of 20 and 3, respectively. Other components (o.c.) such as the $11/2^+$ (4.43 MeV) and the $3/2^-$ (4.72 MeV) excited ^{21}Ne states around 4.5 MeV were included in the calculation (e). See text for details.
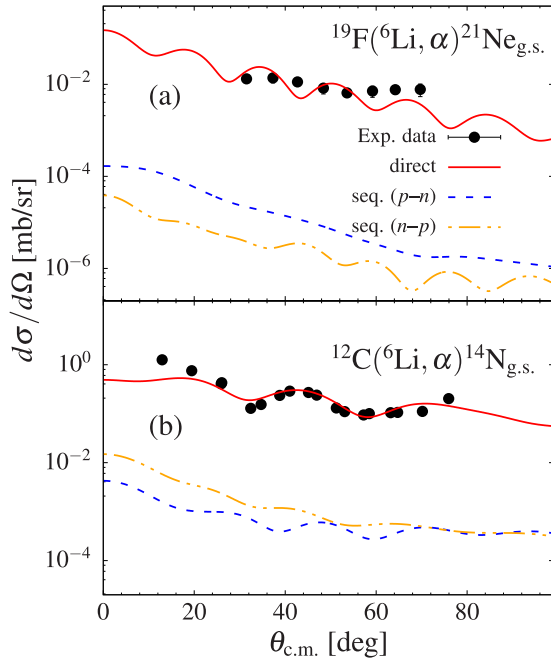
FIG. 12. Comparison between the direct and sequential *np*-transfer mechanisms of the *np*-cluster angular distribution for the ^{19}F(^{6}Li, ^{4}He$_{g.s.}$) ^{21}Ne$_{g.s.}$ (a) and ^{12}C(^{6}Li, ^{4}He$_{g.s.}$) ^{14}N$_{g.s.}$ (b) reactions.

were somewhat lower than the experimental data. The cross sections for these excited states may have contributions from other states or a possible background component. The theoretical angular distributions of all possible contributing direct reaction channels in each case were obtained in the present CRC calculations. However, even the incoherent sums of these components are below the experimental data. Further studies of transfer reactions populating these states can be important to understand a possible quenching of the isoscalar *np* transfer in *sd*-shell nuclei, as also observed in Ref. [40].

B. Two-step *np*-transfer reaction

The sequential *np*-transfer mechanism in the ^{12}C(^{6}Li, α) ^{14}N* and ^{19}F(^{6}Li, α) ^{21}Ne* reactions was investigated with the coupled-channels Born approximation (CCBA) approach. The prior exact finite-range representation was used in the calculations with the code FRESCO [12,28]. Two different paths were considered in the sequential transfer mechanism. In the first path, a valence neutron in ^{6}Li is transferred to the target nucleus, and then a proton is transferred sequentially in an intermediate partition. The second path corresponds to an inverted order of neutron and proton transfers. In both cases, the intermediate partition involves an unbound projectilelike nucleus (^{5}He or ^{5}Li). However, in the present calculations it is assumed that the reaction takes place just before the unbound particle decays.

The OM potentials for the initial and final partitions were the same ones used in the direct *np*-transfer calculations. The SPP interaction was used for the intermediate partitions with the strength coefficients $N_r = 1.0$ and $N_i = 0.78$ for the real and imaginary parts, respectively. The single-particle wave
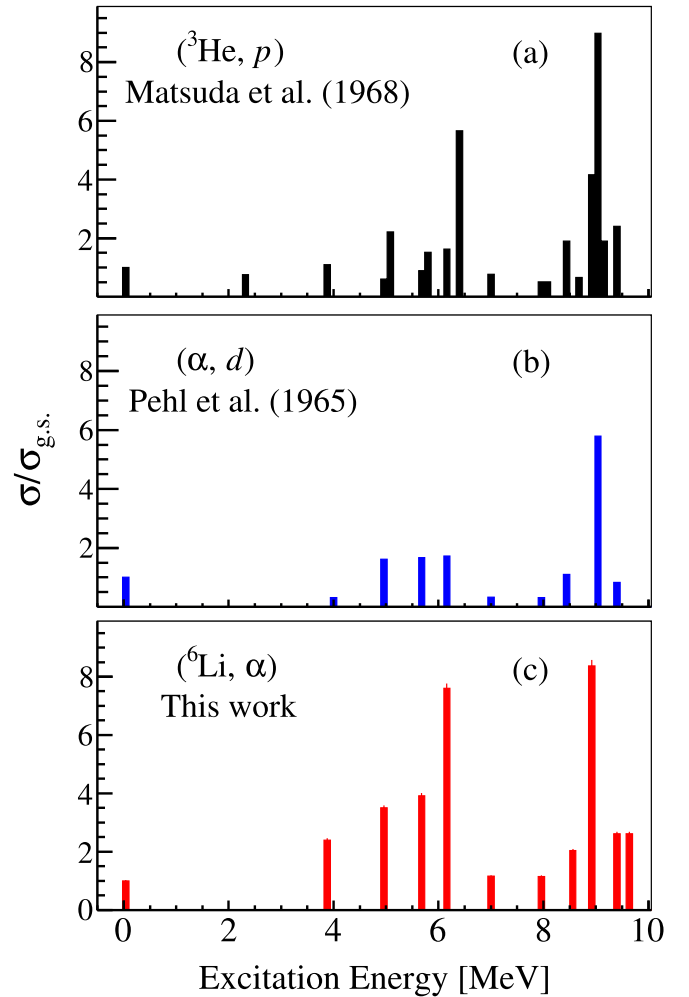

FIG. 13. Comparison of *np*-transfer probes. The height of the histogram bars corresponds to the ratio between the angular-integrated cross section of the excited state and the ground state. The (^{3}He, *p*) data (a) were extracted from Ref. [47], and the (α, *d*) data (b) from Ref. [48].

functions for the target and projectile overlaps were generated from Woods-Saxon potentials with reduced radii and diffuseness set to typical values of 1.20 fm and 0.60 fm, respectively. The depths of these potentials were varied to fit the experimental one-neutron and one-proton binding energies. The spectroscopic amplitudes for the single-particle wave functions of the *p*-valence and *n*-valence particles were determined from shell-model calculations. These structure calculations were carried out considering the same model space and effective interaction used in the direct *np*-transfer calculation presented in the previous section.

The cross sections obtained from the sequential *np*-transfer mechanism underpredict the experimental data, of both ^{12}C(^{6}Li, α) ^{14}N* and ^{19}F(^{6}Li, α) ^{21}Ne* reactions, by several orders of magnitude. For example, Fig. 12(b) shows the result for the sequential transfer of *n*-*p* and *p*-*n* paths, in the ^{6}Li + ^{12}C system, populating the ^{14}N ground state. As can be seen, the sequential transfers are two orders of magnitude smaller than the experimental data and the direct *np*-transfer
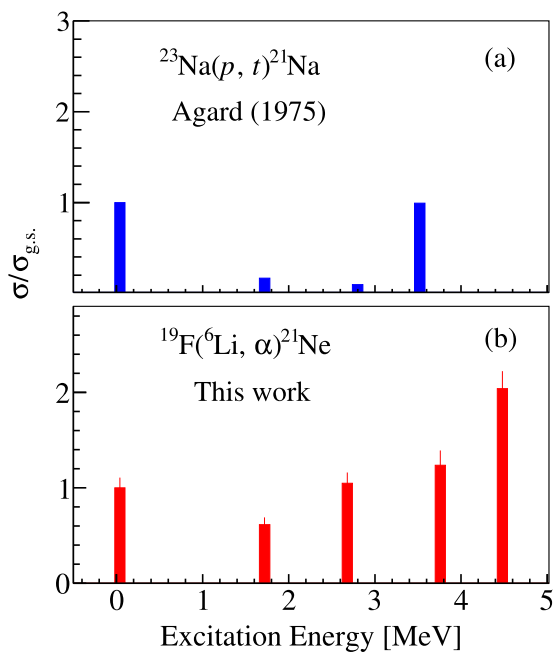
FIG. 14. Comparison of states populated in the mirror nuclei ^{21}Na (a) and ^{21}Ne (b) via nn-transfer and np-transfer reactions, respectively. The height of the histogram bars corresponds to the ratio between the angular-integrated cross section of the excited state and the ground state. The ^{23}Na$(p, t)^{21}$Na data was extracted from Ref. [51].

angular distributions. This result provides a strong evidence of the isoscalar two-nucleon correlation in the ^{14}N excited states. A similar result was observed in the ^{19}F$(^6$Li$, \alpha)^{21}$Ne* reaction. The sequential mechanism is at least two orders of magnitude smaller than the data and the direct transfer prediction, as shown in Fig. 12(a). Although the cross sections with the ^{19}F target are smaller than for the ^{12}C case, the direct np transfer remains dominant over the sequential transfer mechanism in both systems. However, it has been observed that the two-neutron sequential transfer plays a significant role in the reaction mechanism involving medium-mass nuclei such as ^{28}Si [41] or ^{64}Ni [42]. Therefore, the interplay between direct and sequential two-nucleon transfer might be intrinsically related to the nuclear structure of the target nuclei.

IV. DISCUSSION

The interplay between direct and sequential two-nucleon transfer has been widely discussed in the past. In particular, the enhancement of the direct two-nucleon transfer over the sequential transfer mechanism has important consequences in pairing correlations in nuclei [5,43]. In the case of a dominant direct reaction process, the correlation between nucleon pairs is expected to be significant, while a strong sequential transfer mechanism leads to a weak nucleon pair correlation. Thus, the observed dominance of direct two-nucleon transfer in this work suggests a strong np correlation in the ^{12}C$(^6$Li$, \alpha)^{14}$N* and ^{19}F$(^6$Li$, \alpha)^{21}$Ne* reactions. The present results are consistent with quasielastic knockout experiments using high-energy electrons [$(e, e'pp)$, $(e, e'pn)$] on ^{4}He and

^{12}C targets [44,45]. These experiments demonstrated that the correlation between np pairs in such a light nuclei is nearly 20 times more prevalent than that between pp pairs and, by inference, nn pairs.

In the past, the mechanism of the ^{12}C$(^6$Li$, \alpha)^{14}$N* reaction has been interpreted as a multistep process [31]. A poor description of the ground state angular distribution with the CCBA approach was associated with a significant contribution of the sequential transfer mechanism. However, only excited states in the target and projectile nuclei were taken into account as well as a few specifics states in the ^{14}N. In our work, it was observed that the contribution in the transfer reaction cross sections due to couplings with excited states in the target nucleus was small. On the other hand, the coupling with the 3_1^+ (2.19 MeV) excited state in ^{6}Li exhibits a stronger contribution. The full coupling scheme assumed for the target overlap affected all the reaction channels, mainly the couplings with high-excitation energy states in ^{14}N (e.g. continuum states) that are explicitly considered in the final partition. Therefore, a consistent analysis about the interplay between direct and sequential two-nucleon transfer requires a robust coupling mechanism including states of both initial and final partitions.

The np-transfer reaction can be investigated in experiments with the $(^3$He$, p)$, (α, d), and $(^6$Li$, \alpha)$ probes. On the one hand, the (α, d) and $(^6$Li$, \alpha)$ probes predominantly transfer isoscalar np pairs (deuteronlike particle). On the other hand, the $(^3$He$, p)$ reaction induces both isoscalar and isovector np transfers in nuclei. Figure 13 shows a comparison of the three probes using a ^{12}C target. The horizontal axis corresponds to the ^{14}N excitation energy and the vertical axis is the ratio between the angular-integrated cross sections of the excited and ground states. A clear difference in the spectra is seen in the missing $T = 1$ states [46] (2.31 MeV and many above 8 MeV) in the (α, d) [Fig. 13(b)] and $(^6$Li$, \alpha)$ [Fig. 13(c)] data. It is also interesting to see the ratio of the first 1_1^+ (3.95 MeV) state in the three cases. While the $(^6$Li$, \alpha)$ probe exhibit a ratio of about 3, only about half of this value is observed in the $(^3$He$, p)$ [Fig. 13(a)] reaction and even less for the (α, d) case. The two main reasons for this difference are the strong $T = 0$ filter and good momentum matching of the $(^6$Li$, \alpha)$ probe. In particular, the momentum matching enhanced for low L values in the $(^6$Li$, \alpha)$ reaction can be observed in the strength of excited states with respect to the (α, d) probe.

In the case of np transfer in a ^{19}F target, the nuclear structure of the involved nuclei plays an important role in the reaction mechanism. For instance, the proton-neutron asymmetry in nuclei increases the Fermi level difference and, consequently, reduces the np-transfer cross section. This effect has interesting implications in studies of asymmetric nuclear matter in stellar media [49]. In particular, np-transfer cross sections in ^{19}F are two orders of magnitude smaller than transfers in the symmetric nucleus ^{12}C. Apparently, an extra neutron in the $1d_{5/2}$ shell provides a Pauli blocking effect in the np-transfer process. Nevertheless, the dominance of the direct-reaction mechanism in ^{19}F also suggests a significant np correlation even in such a asymmetric nucleus. The dominance of the np correlation in asymmetric nuclei has also been

TABLE V. Spectroscopic amplitudes for the projectile and target overlaps wave functions considered in the *np*-transfer calculation in the ^{19}F(^{6}Li, ^{4}He) ^{21}Ne reaction.

TABLE V. (*Continued.*)

Initial state	N	L	S	J	Final state	S.A.
^{19}F$_{g.s.}$(1/2$^+$)	2	0	1	1	^{21}Ne$_{g.s.}$(3/2$^+$)	−0.016
^{19}F$_{g.s.}$(1/2$^+$)	1	2	1	1	^{21}Ne$_{g.s.}$(3/2$^+$)	0.070
^{19}F$_{g.s.}$(1/2$^+$)	3	0	1	1	^{21}Ne$_{g.s.}$(3/2$^+$)	0.135
^{19}F$_{g.s.}$(1/2$^+$)	2	2	1	1	^{21}Ne$_{g.s.}$(3/2$^+$)	−0.049
^{19}F$_{g.s.}$(1/2$^+$)	2	2	1	2	^{21}Ne$_{g.s.}$(3/2$^+$)	0.028
^{19}F$_{g.s.}$(1/2$^+$)	2	2	1	2	^{21}Ne$_{0.35}$(5/2$^+$)	−0.110
^{19}F$_{g.s.}$(1/2$^+$)	2	2	1	3	^{21}Ne$_{0.35}$(5/2$^+$)	−0.101
^{19}F$_{g.s.}$(1/2$^+$)	2	2	1	3	^{21}Ne$_{1.75}$(7/2$^+$)	0.131
^{19}F$_{g.s.}$(1/2$^+$)	2	1	1	0	^{21}Ne$_{2.79}$(1/2$^-$)	0.079
^{19}F$_{g.s.}$(1/2$^+$)	2	1	1	1	^{21}Ne$_{2.79}$(1/2$^-$)	0.117
^{19}F$_{g.s.}$(1/2$^+$)	2	0	1	1	^{21}Ne$_{2.79}$(1/2$^+$)	−0.007
^{19}F$_{g.s.}$(1/2$^+$)	1	2	1	1	^{21}Ne$_{2.79}$(1/2$^+$)	0.032
^{19}F$_{g.s.}$(1/2$^+$)	3	0	1	1	^{21}Ne$_{2.79}$(1/2$^+$)	−0.202
^{19}F$_{g.s.}$(1/2$^+$)	2	2	1	1	^{21}Ne$_{2.79}$(1/2$^+$)	−0.023
^{19}F$_{g.s.}$(1/2$^+$)	2	1	1	1	^{21}Ne$_{3.66}$(3/2$^-$)	−0.006
^{19}F$_{g.s.}$(1/2$^+$)	2	1	1	2	^{21}Ne$_{3.66}$(3/2$^-$)	0.112
^{19}F$_{g.s.}$(1/2$^+$)	1	3	1	2	^{21}Ne$_{3.66}$(3/2$^-$)	0.043
^{19}F$_{g.s.}$(1/2$^+$)	2	2	1	2	^{21}Ne$_{3.74}$(5/2$^+$)	0.063
^{19}F$_{g.s.}$(1/2$^+$)	2	2	1	3	^{21}Ne$_{3.74}$(5/2$^+$)	0.009
^{19}F$_{g.s.}$(1/2$^+$)	2	1	1	2	^{21}Ne$_{3.88}$(5/2$^-$)	−0.012
^{19}F$_{g.s.}$(1/2$^+$)	1	3	1	2	^{21}Ne$_{3.88}$(5/2$^-$)	−0.005
^{19}F$_{g.s.}$(1/2$^+$)	1	3	1	3	^{21}Ne$_{3.88}$(5/2$^-$)	0.076
^{19}F$_{g.s.}$(1/2$^+$)	2	2	1	2	^{21}Ne$_{4.53}$(5/2$^+$)	0.067
^{19}F$_{g.s.}$(1/2$^+$)	2	2	1	3	^{21}Ne$_{4.53}$(5/2$^+$)	−0.073
^{19}F$_{g.s.}$(1/2$^+$)	2	0	1	1	^{21}Ne$_{4.69}$(3/2$^+$)	−0.001
^{19}F$_{g.s.}$(1/2$^+$)	1	2	1	1	^{21}Ne$_{4.69}$(3/2$^+$)	0.003
^{19}F$_{g.s.}$(1/2$^+$)	3	0	1	1	^{21}Ne$_{4.69}$(3/2$^+$)	0.038
^{19}F$_{g.s.}$(1/2$^+$)	2	2	1	1	^{21}Ne$_{4.69}$(3/2$^+$)	−0.013
^{19}F$_{g.s.}$(1/2$^+$)	2	2	1	2	^{21}Ne$_{4.69}$(3/2$^+$)	0.096
^{19}F$_{g.s.}$(1/2$^+$)	2	1	1	1	^{21}Ne$_{4.69}$(3/2$^+$)	0.009
^{19}F$_{g.s.}$(1/2$^+$)	2	1	1	2	^{21}Ne$_{4.69}$(3/2$^+$)	−0.017
^{19}F$_{g.s.}$(1/2$^+$)	1	3	1	2	^{21}Ne$_{4.69}$(3/2$^+$)	−0.006
^{19}F$_{0.197}$(5/2$^+$)	2	0	1	1	^{21}Ne$_{g.s.}$(3/2$^+$)	0.003
^{19}F$_{0.197}$(5/2$^+$)	1	2	1	1	^{21}Ne$_{g.s.}$(3/2$^+$)	−0.013
^{19}F$_{0.197}$(5/2$^+$)	3	0	1	1	^{21}Ne$_{g.s.}$(3/2$^+$)	0.028
^{19}F$_{0.197}$(5/2$^+$)	2	2	1	1	^{21}Ne$_{g.s.}$(3/2$^+$)	0.011
^{19}F$_{0.197}$(5/2$^+$)	2	2	1	2	^{21}Ne$_{g.s.}$(3/2$^+$)	0.402
^{19}F$_{0.197}$(5/2$^+$)	2	2	1	3	^{21}Ne$_{g.s.}$(3/2$^+$)	−0.278
^{19}F$_{0.197}$(5/2$^+$)	2	2	1	3	^{21}Ne$_{g.s.}$(3/2$^+$)	0.016
^{19}F$_{0.197}$(5/2$^+$)	2	0	1	1	^{21}Ne$_{0.35}$(5/2$^+$)	0.007
^{19}F$_{0.197}$(5/2$^+$)	1	2	1	1	^{21}Ne$_{0.35}$(5/2$^+$)	−0.029
^{19}F$_{0.197}$(5/2$^+$)	3	0	1	1	^{21}Ne$_{0.35}$(5/2$^+$)	−0.006
^{19}F$_{0.197}$(5/2$^+$)	2	2	1	1	^{21}Ne$_{0.35}$(5/2$^+$)	0.027
^{19}F$_{0.197}$(5/2$^+$)	2	2	1	2	^{21}Ne$_{0.35}$(5/2$^+$)	0.009
^{19}F$_{0.197}$(5/2$^+$)	2	2	1	3	^{21}Ne$_{0.35}$(5/2$^+$)	−0.002
^{19}F$_{0.197}$(5/2$^+$)	2	2	1	3	^{21}Ne$_{0.35}$(5/2$^+$)	0.027
^{19}F$_{0.197}$(5/2$^+$)	2	0	1	1	^{21}Ne$_{1.75}$(7/2$^+$)	−0.013
^{19}F$_{0.197}$(5/2$^+$)	1	2	1	1	^{21}Ne$_{1.75}$(7/2$^+$)	0.060
^{19}F$_{0.197}$(5/2$^+$)	3	0	1	1	^{21}Ne$_{1.75}$(7/2$^+$)	0.068
^{19}F$_{0.197}$(5/2$^+$)	2	2	1	1	^{21}Ne$_{1.75}$(7/2$^+$)	−0.029
^{19}F$_{0.197}$(5/2$^+$)	2	2	1	2	^{21}Ne$_{1.75}$(7/2$^+$)	−0.063
^{19}F$_{0.197}$(5/2$^+$)	2	2	1	3	^{21}Ne$_{1.75}$(7/2$^+$)	−0.139
^{19}F$_{0.197}$(5/2$^+$)	2	2	1	3	^{21}Ne$_{1.75}$(7/2$^+$)	0.039
^{19}F$_{0.197}$(5/2$^+$)	2	1	1	2	^{21}Ne$_{2.79}$(1/2$^-$)	0.113
^{19}F$_{0.197}$(5/2$^+$)	1	3	1	2	^{21}Ne$_{2.79}$(1/2$^-$)	0.043
^{19}F$_{0.197}$(5/2$^+$)	1	3	1	3	^{21}Ne$_{2.79}$(1/2$^-$)	0.131
^{19}F$_{0.197}$(5/2$^+$)	2	2	1	2	^{21}Ne$_{2.79}$(1/2$^+$)	0.193
^{19}F$_{0.197}$(5/2$^+$)	2	2	1	3	^{21}Ne$_{2.79}$(1/2$^+$)	−0.124
^{19}F$_{0.197}$(5/2$^+$)	1	4	1	3	^{21}Ne$_{2.79}$(1/2$^+$)	−0.016
^{19}F$_{0.197}$(5/2$^+$)	2	2	1	2	^{21}Ne$_{2.87}$(9/2$^+$)	−0.095
^{19}F$_{0.197}$(5/2$^+$)	2	2	1	3	^{21}Ne$_{2.87}$(9/2$^+$)	−0.117
^{19}F$_{0.197}$(5/2$^+$)	1	4	1	3	^{21}Ne$_{2.87}$(9/2$^+$)	0.017
^{19}F$_{0.197}$(5/2$^+$)	2	1	1	1	^{21}Ne$_{3.66}$(3/2$^-$)	−0.100
^{19}F$_{0.197}$(5/2$^+$)	2	1	1	2	^{21}Ne$_{3.66}$(3/2$^-$)	0.076
^{19}F$_{0.197}$(5/2$^+$)	1	3	1	2	^{21}Ne$_{3.66}$(3/2$^-$)	0.029
^{19}F$_{0.197}$(5/2$^+$)	1	3	1	3	^{21}Ne$_{3.66}$(3/2$^-$)	−0.036
^{19}F$_{0.197}$(5/2$^+$)	2	0	1	1	^{21}Ne$_{3.74}$(5/2$^+$)	−0.007
^{19}F$_{0.197}$(5/2$^+$)	1	2	1	1	^{21}Ne$_{3.74}$(5/2$^+$)	0.032
^{19}F$_{0.197}$(5/2$^+$)	3	0	1	1	^{21}Ne$_{3.74}$(5/2$^+$)	−0.183
^{19}F$_{0.197}$(5/2$^+$)	2	2	1	1	^{21}Ne$_{3.74}$(5/2$^+$)	−0.005
^{19}F$_{0.197}$(5/2$^+$)	2	2	1	2	^{21}Ne$_{3.74}$(5/2$^+$)	0.110
^{19}F$_{0.197}$(5/2$^+$)	2	2	1	3	^{21}Ne$_{3.74}$(5/2$^+$)	−0.115
^{19}F$_{0.197}$(5/2$^+$)	2	2	1	3	^{21}Ne$_{3.74}$(5/2$^+$)	0.030
^{19}F$_{0.197}$(5/2$^+$)	2	1	1	0	^{21}Ne$_{3.88}$(5/2$^-$)	0.076
^{19}F$_{0.197}$(5/2$^+$)	2	1	1	1	^{21}Ne$_{3.88}$(5/2$^-$)	0.056
^{19}F$_{0.197}$(5/2$^+$)	2	1	1	2	^{21}Ne$_{3.88}$(5/2$^-$)	0.012
^{19}F$_{0.197}$(5/2$^+$)	1	3	1	2	^{21}Ne$_{3.88}$(5/2$^-$)	0.005
^{19}F$_{0.197}$(5/2$^+$)	1	3	1	3	^{21}Ne$_{3.88}$(5/2$^-$)	0.052
^{19}F$_{0.197}$(5/2$^+$)	2	2	1	3	^{21}Ne$_{4.43}$(11/2$^+$)	0.117
^{19}F$_{0.197}$(5/2$^+$)	1	4	1	3	^{21}Ne$_{4.43}$(11/2$^+$)	−0.037
^{19}F$_{0.197}$(5/2$^+$)	2	0	1	1	^{21}Ne$_{4.53}$(5/2$^+$)	0.0005
^{19}F$_{0.197}$(5/2$^+$)	1	2	1	1	^{21}Ne$_{4.53}$(5/2$^+$)	−0.002
^{19}F$_{0.197}$(5/2$^+$)	3	0	1	1	^{21}Ne$_{4.53}$(5/2$^+$)	−0.199
^{19}F$_{0.197}$(5/2$^+$)	2	2	1	1	^{21}Ne$_{4.53}$(5/2$^+$)	0.022
^{19}F$_{0.197}$(5/2$^+$)	2	2	1	2	^{21}Ne$_{4.53}$(5/2$^+$)	0.011
^{19}F$_{0.197}$(5/2$^+$)	2	2	1	3	^{21}Ne$_{4.53}$(5/2$^+$)	−0.042
^{19}F$_{0.197}$(5/2$^+$)	2	2	1	3	^{21}Ne$_{4.53}$(5/2$^+$)	−0.041
^{19}F$_{0.197}$(5/2$^+$)	2	0	1	1	^{21}Ne$_{4.69}$(3/2$^+$)	−0.002
^{19}F$_{0.197}$(5/2$^+$)	1	2	1	1	^{21}Ne$_{4.69}$(3/2$^+$)	0.008
^{19}F$_{0.197}$(5/2$^+$)	3	0	1	1	^{21}Ne$_{4.69}$(3/2$^+$)	0.250
^{19}F$_{0.197}$(5/2$^+$)	2	2	1	1	^{21}Ne$_{4.69}$(3/2$^+$)	−0.007
^{19}F$_{0.197}$(5/2$^+$)	2	2	1	2	^{21}Ne$_{4.69}$(3/2$^+$)	0.080
^{19}F$_{0.197}$(5/2$^+$)	2	2	1	3	^{21}Ne$_{4.69}$(3/2$^+$)	0.036
^{19}F$_{0.197}$(5/2$^+$)	2	2	1	3	^{21}Ne$_{4.69}$(3/2$^+$)	0.002
^{19}F$_{0.197}$(5/2$^+$)	2	1	1	1	^{21}Ne$_{4.73}$(3/2$^-$)	0.005
^{19}F$_{0.197}$(5/2$^+$)	2	1	1	2	^{21}Ne$_{4.73}$(3/2$^-$)	−0.051
^{19}F$_{0.197}$(5/2$^+$)	1	3	1	2	^{21}Ne$_{4.73}$(3/2$^-$)	−0.020
^{19}F$_{0.197}$(5/2$^+$)	1	3	1	3	^{21}Ne$_{4.73}$(3/2$^-$)	−0.032
^{19}F$_{2.78}$(9/2$^+$)	2	2	1	3	^{21}Ne$_{g.s.}$(3/2$^+$)	−0.259
^{19}F$_{2.78}$(9/2$^+$)	1	4	1	4	^{21}Ne$_{g.s.}$(3/2$^+$)	0.017
^{19}F$_{2.78}$(9/2$^+$)	2	2	1	2	^{21}Ne$_{0.35}$(5/2$^+$)	−0.007
^{19}F$_{2.78}$(9/2$^+$)	2	2	1	3	^{21}Ne$_{0.35}$(5/2$^+$)	−0.035
^{19}F$_{2.78}$(9/2$^+$)	1	4	1	3	^{21}Ne$_{0.35}$(5/2$^+$)	0.030
^{19}F$_{2.78}$(9/2$^+$)	2	0	1	1	^{21}Ne$_{1.75}$(7/2$^+$)	0.0002

TABLE V. (*Continued.*)

Initial state	N	L	S	J	Final state	S.A.
^{19}F$_{2.78}(9/2^+)$	1	2	1	1	^{21}Ne$_{1.75}(7/2^+)$	-0.001
^{19}F$_{2.78}(9/2^+)$	3	0	1	1	^{21}Ne$_{1.75}(7/2^+)$	-0.160
^{19}F$_{2.78}(9/2^+)$	2	2	1	1	^{21}Ne$_{1.75}(7/2^+)$	0.014
^{19}F$_{2.78}(9/2^+)$	2	2	1	2	^{21}Ne$_{1.75}(7/2^+)$	-0.025
^{19}F$_{2.78}(9/2^+)$	2	2	1	3	^{21}Ne$_{1.75}(7/2^+)$	0.053
^{19}F$_{2.78}(9/2^+)$	1	4	1	3	^{21}Ne$_{1.75}(7/2^+)$	-0.018
^{19}F$_{2.78}(9/2^+)$	2	0	1	1	^{21}Ne$_{2.87}(9/2^+)$	-0.007
^{19}F$_{2.78}(9/2^+)$	1	2	1	1	^{21}Ne$_{2.87}(9/2^+)$	0.030
^{19}F$_{2.78}(9/2^+)$	3	0	1	1	^{21}Ne$_{2.87}(9/2^+)$	-0.020
^{19}F$_{2.78}(9/2^+)$	2	2	1	1	^{21}Ne$_{2.87}(9/2^+)$	-0.019
^{19}F$_{2.78}(9/2^+)$	2	2	1	2	^{21}Ne$_{2.87}(9/2^+)$	-0.075
^{19}F$_{2.78}(9/2^+)$	2	2	1	3	^{21}Ne$_{2.87}(9/2^+)$	-0.024
^{19}F$_{2.78}(9/2^+)$	1	4	1	3	^{21}Ne$_{2.87}(9/2^+)$	-0.032
^{19}F$_{2.78}(9/2^+)$	1	3	1	3	^{21}Ne$_{3.66}(3/2^-)$	0.064
^{19}F$_{2.78}(9/2^+)$	2	2	1	2	^{21}Ne$_{3.74}(5/2^+)$	-0.055
^{19}F$_{2.78}(9/2^+)$	2	2	1	3	^{21}Ne$_{3.74}(5/2^+)$	0.088
^{19}F$_{2.78}(9/2^+)$	1	4	1	3	^{21}Ne$_{3.74}(5/2^+)$	0.013
^{19}F$_{2.78}(9/2^+)$	2	1	1	2	^{21}Ne$_{3.88}(5/2^-)$	-0.060
^{19}F$_{2.78}(9/2^+)$	1	3	1	3	^{21}Ne$_{3.88}(5/2^-)$	-0.036
^{19}F$_{2.78}(9/2^+)$	2	0	1	1	^{21}Ne$_{4.43}(11/2^+)$	0.011
^{19}F$_{2.78}(9/2^+)$	1	2	1	1	^{21}Ne$_{4.43}(11/2^+)$	-0.047
^{19}F$_{2.78}(9/2^+)$	3	0	1	1	^{21}Ne$_{4.43}(11/2^+)$	0.003
^{19}F$_{2.78}(9/2^+)$	2	2	1	1	^{21}Ne$_{4.43}(11/2^+)$	0.006
^{19}F$_{2.78}(9/2^+)$	2	2	1	2	^{21}Ne$_{4.43}(11/2^+)$	0.022
^{19}F$_{2.78}(9/2^+)$	2	2	1	3	^{21}Ne$_{4.43}(11/2^+)$	0.056
^{19}F$_{2.78}(9/2^+)$	1	4	1	3	^{21}Ne$_{4.43}(11/2^+)$	0.009
^{19}F$_{2.78}(9/2^+)$	2	2	1	2	^{21}Ne$_{4.53}(5/2^+)$	-0.068
^{19}F$_{2.78}(9/2^+)$	2	2	1	3	^{21}Ne$_{4.53}(5/2^+)$	-0.224
^{19}F$_{2.78}(9/2^+)$	1	4	1	3	^{21}Ne$_{4.53}(5/2^+)$	0.016
^{19}F$_{2.78}(9/2^+)$	2	2	1	3	^{21}Ne$_{4.69}(3/2^-)$	0.164
^{19}F$_{2.78}(9/2^+)$	1	4	1	4	^{21}Ne$_{4.69}(3/2^-)$	-0.024
^{19}F$_{2.78}(9/2^+)$	1	3	1	3	^{21}Ne$_{4.73}(3/2^-)$	-0.021

observed in proton and neutron knockout experiments using high energy electrons [50].

Since the availability of np-transfer data populating states in ^{21}Ne is still very scarce, the integrated cross sections were compared with data obtained with the isobaric mirror ^{21}Na nucleus. Figure 14 shows a comparison of the cross section ratio with the ground state for the np and nn transfer reactions. It is important to mention that the isovector g.s. → g.s. cross section in the ^{21}Na case is about two orders of magnitude stronger than for the np transfer to ^{21}Ne. However, the ratio of the first two excited states in ^{21}Na [Fig. 14(a)] is hindered with respect the ground-state cross section. A comparison with the analog states [Fig. 14(b)] exhibits a clear imbalance of the cross section strengths. Further studies of both np and nn reactions will be needed to fully understand the reaction mechanism of two-nucleon transfer in sd-shell nuclei.

V. SUMMARY

Elastic scattering and isoscalar np-transfer reactions induced by a 20 MeV ^{6}Li beam on ^{12}C and ^{19}F targets were measured. Angular distributions of several excited states in the residual ^{14}N and ^{21}Ne nuclei were obtained in this experi-

ment. Transfer reaction cross sections with the ^{12}C target were systematically higher by two orders of magnitude with respect to np transfers in the ^{19}F nucleus.

The interplay between direct and sequential np-transfer mechanism was investigated with exact finite-range CRC calculations. In the ^{12}C data, in total 21 (bound and unbound) states in ^{14}N were included in the CRC calculations. A reasonable good agreement with the data was achieved for the low-lying and a few resonance states. Due to the higher density of states in the ^{19}F and ^{21}Ne partner nuclei, the coupling scheme used for the CRC calculations included several transitions from the ground state and excited states in ^{19}F to many states in the ^{21}Ne residual nucleus. A good agreement with the experimental angular distributions was obtained for most of the cases. However, the angular distributions for states at higher excitation energies were lower than the experimental data. Further studies with high-resolution experiments will be required to separate the different excited states populated in ^{21}Ne and to reduce the background component. These studies will also be important to fully understand the isoscalar np-transfer process in asymmetric sd-shell nuclei.

The sequential np-transfer mechanism was investigated with CCBA calculations. Angular distributions of the sequential transfer are two orders of magnitude smaller than the direct transfer in the ^{12}C$(^6$Li$, \alpha)$ ^{14}N* and ^{19}F$(^6$Li$, \alpha)$ ^{21}Ne* reactions. This result suggests an important np correlation in both systems.

The $(^6$Li$, \alpha)$ probe is a strong isoscalar np-transfer filter. The probe has a better momentum matching for low L transfers than the usual (α, d) reaction used in np-transfer studies. Future experiments to investigate the role of np correlations in light asymmetric nuclei are planned with both $(^6$Li$, \alpha)$ (isoscalar) and $(^3$He$, p)$ (isovector/isocalar) reaction probes.

APPENDIX

Tables IV and V list spectroscopic amplitudes for the valence np cluster, considering the active orbits $p_{1/2}$, $d_{5/2}$, and $s_{1/2}$ as model space for both proton and neutron.

[1] E. Vigezzi *et al.*, Nucl. Phys. A **752**, 600 (2005), Proceedings of the 22nd International Nuclear Physics Conference (Part 2).

[2] W. Guo *et al.*, Nucl. Phys. A **986**, 18 (2019).

[3] E. Caurier, J. Menéndez, F. Nowacki, and A. Poves, Phys. Rev. Lett. **100**, 052503 (2008).

[4] V. Cirigliano, W. Dekens, J. deVries, M. L. Graesser, E. Mereghetti, S. Pastore, and U. vanKolck, Phys. Rev. Lett. **120**, 202001 (2018).

[5] D. M. Brink and R. A. Broglia, *Nuclear Superfluidity: Pairing in Finite Systems*, Cambridge Monographs on Particle Physics, Nuclear Physics and Cosmology (Cambridge University Press, Cambridge, 2005).

[6] F. Cappuzzello *et al.*, Nat. Commun. **6**, 6743 (2015).

[7] D. K. Scott *et al.*, Phys. Rev. Lett. **34**, 895 (1975).

[8] B. F. Bayman and J. Chen, Phys. Rev. C **26**, 1509 (1982).

[9] G. Potel, F. Barranco, F. Marini, A. Idini, E. Vigezzi, and R. A. Broglia, Phys. Rev. Lett. **107**, 092501 (2011).

[10] J. L. Ferreira, D. Carbone, M. Cavallaro, N. N. Deshmukh, C. Agodi, G. A. Brischetto, S. Calabrese, F. Cappuzzello, E. N. Cardozo, I. Ciraldo, M. Cutuli, M. Fisichella, A. Foti, L. La Fauci, O. Sgouros, V. Soukeras, A. Spatafora, D. Torresi, and J. Lubian (NUMEN Collaboration), Phys. Rev. C **103**, 054604 (2021).

[11] D. Carbone, J. L. Ferreira, S. Calabrese, F. Cappuzzello, M. Cavallaro, A. Hacisalihoglu, H. Lenske, J. Lubian, R. I. Magnana Vsevolodovna, E. Santopinto, C. Agodi, L. Acosta, D. Bonanno, T. Borello-Lewin, I. Boztosun, G. A. Brischetto, S. Burrello, D. Calvo, E. R. ChavezLomeli, I. Ciraldo, *et al.* (NUMEN Collaboration), Phys. Rev. C **102**, 044606 (2020).

[12] I. J. Thompson, Comput. Phys. Rep. **7**, 167 (1988).

[13] E. Perez-Ferreira *et al.*, Nucl. Instrum. Methods Phys. Res. **220**, 37 (1984).

[14] NuShellX for Windows and Linux, http://www.garsington.eclipse.co.uk/.

[15] M. Cavallaro, F. Cappuzzello, M. Bondi, D. Carbone, V. N. Garcia, A. Gargano, S. M. Lenzi, J. Lubian, C. Agodi, F. Azaiez, M. De Napoli, A. Foti, S. Franchoo, R. Linares, D. Nicolosi, M. Niikura, J. A. Scarpaci, and S. Tropea, Phys. Rev. C **88**, 054601 (2013).

[16] J. B. McGrory and B. H. Wildenthal, Phys. Rev. C **7**, 974 (1973).

[17] D. Carbone, J. L. Ferreira, F. Cappuzzello, J. Lubian, C. Agodi, M. Cavallaro, A. Foti, A. Gargano, S. M. Lenzi, R. Linares, and G. Santagati, Phys. Rev. C **95**, 034603 (2017).

[18] M. Moshinsky, Nucl. Phys. **13**, 104 (1959).

[19] L. C. Chamon, D. Pereira, M. S. Hussein, M. A. Cândido Ribeiro, and D. Galetti, Phys. Rev. Lett. **79**, 5218 (1997).

[20] D. Sousa *et al.*, Nucl. Phys. A **836**, 1 (2010).

[21] L. Gasques, L. Chamon, P. Gomes, and J. Lubian, Nucl. Phys. A **764**, 135 (2006).

[22] J. Carter *et al.*, Nucl. Phys. A **591**, 349 (1995).

[23] J. England *et al.*, Nucl. Phys. A **284**, 29 (1977).

[24] M. Morais and R. Lichtenthäler, Nucl. Phys. A **857**, 1 (2011).

[25] J. L. Ferreira *et al.*, Eur. Phys. J. A **55**, 94 (2019).

[26] U. Umbelino, K. C. C. Pires, R. Lichtenthaler, V. Scarduelli, G. A. Scotton, A. Lepine-Szily, V. Guimaraes, J. Lubian, B. Paes, J. L. Ferreira, M. A. G. Alvarez, J. M. B. Shorto, S. Appannababu, M. Assuncao, R. P. Condori, and V. Morcelle, Phys. Rev. C **99**, 064617 (2019).

[27] Z. Pastuovic *et al.*, Nucl. Instrum. Methods Phys. Res., Sect. B **136-138**, 81 (1998).

[28] I. J. Thompson, FRESCO code, http://www.fresco.org.uk/.

[29] M. F. Werby, M. B. Greenfield, K. W. Kemper, D. L. McShan, and S. Edwards, Phys. Rev. C **8**, 106 (1973).

[30] A. J. Mendez, K. W. Kemper, P. V. Green, P. L. Kerr, E. G. Myers, E. L. Reber, and D. Robson, Phys. Rev. C **51**, 651 (1995).

[31] F. Maréchal, T. L. Drummer, and K. W. Kemper, Phys. Rev. C **61**, 064607 (2000).

[32] P. Rath *et al.*, Nucl. Phys. A **874**, 14 (2012).

[33] P. K. Rath, S. Santra, N. L. Singh, R. Tripathi, V. V. Parkar, B. K. Nayak, K. Mahata, R. Palit, S. Kumar, S. Mukherjee, S. Appannababu, and R. K. Choudhury, Phys. Rev. C **79**, 051601(R) (2009).

[34] C. Beck, F. A. Souza, N. Rowley, S. J. Sanders, N. Aissaoui, E. E. Alonso, P. Bednarczyk, N. Carlin, S. Courtin, A. Diaz-Torres, A. Dummer, F. Haas, A. Hachem, K. Hagino, F. Hoellinger, R. V. F. Janssens, N. Kintz, R. Liguori Neto, E. Martin, M. M. Moura, M. G. Munhoz, P. Papka, M. Rousseau, A. Sanchezi Zafra, O. Stezowski, A. A. Suaide, E. M. Szanto, A. Szanto de Toledo, S. Szilner, and J. Takahashi, Phys. Rev. C **67**, 054602 (2003).

[35] M. R. Cortes, J. Rangel, J. L. Ferreira, J. Lubian, and L. F. Canto, Phys. Rev. C **102**, 064628 (2020).

[36] N. Austern *et al.*, Phys. Rep. **154**, 125 (1987).

[37] T. Matsumoto, T. Kamizato, K. Ogata, Y. Iseri, E. Hiyama, M. Kamimura, and M. Yahiro, Phys. Rev. C **68**, 064607 (2003).

[38] I. J. Thompson and F. M. Nunes, *Nuclear Reactions for Astrophysics: Principles, Calculation and Applications of Low-Energy Reactions* (Cambridge University Press, Cambridge, 2009).

[39] F. Ajzenberg-Selove, Nucl. Phys. A **475**, 1 (1987).

[40] H. Nann and B. H. Wildenthal, Phys. Rev. Lett. **37**, 1129 (1976).

[41] E. N. Cardozo, J. Lubian, R. Linares, F. Cappuzzello, D. Carbone, M. Cavallaro, J. L. Ferreira, A. Gargano, B. Paes, G. Santagati, Phys. Rev. C **97**, 064611 (2018).

[42] B. Paes, G. Santagati, R. M. Vsevolodovna, F. Cappuzzello, D. Carbone, E. N. Cardozo, M. Cavallaro, H. Garcia-Tecocoatzi, A. Gargano, J. L. Ferreira, S. M. Lenzi, R. Linares, E. Santopinto, A. Vitturi, J. Lubian, Phys. Rev. C **96**, 044612 (2017).

[43] W. von Oertzen and A. Vitturi, Rep. Prog. Phys. **64**, 1247 (2001).

[44] I. Korover *et al.* (Jefferson Lab Hall A Collaboration), Phys. Rev. Lett. **113**, 022501 (2014).

[45] R. Subedi *et al.*, Science **320**, 1476 (2008).

[46] F. Ajzenberg-Selove, Nucl. Phys. A **268**, 1 (1976).

[47] K. Matsuda *et al.*, J. Phys. Soc. Jpn. **25**, 1207 (1968).

[48] R. H. Pehl, E. Rivet, J. Cerny, and B. G. Harvey, Phys. Rev. **137**, B114 (1965).

[49] T. Sogo, G. Röpke, and P. Schuck, Phys. Rev. C **82**, 034322 (2010).

[50] The CLAS Collaboration, Nature (London) **560**, 617 (2018).

[51] M. Agard, Etude de la reaction ^{23}Na(p, t)^{21}Na, Ph.D. thesis, Universite Scientifique et Medicale de Grenoble, 1975 (unpublished).